

Oxysulfides $\text{Ln}_2\text{Ti}_2\text{S}_2\text{O}_5$ as Stable Photocatalysts for Water Oxidation and Reduction under Visible-Light Irradiation

Akio Ishikawa,[†] Tsuyoshi Takata,[†] Tadaaki Matsumura,[‡] Junko N. Kondo,[†] Michikazu Hara,[†] Hisayoshi Kobayashi,[§] and Kazunari Domen^{*,||}

Chemical Resources Laboratory, Tokyo Institute of Technology, Nagatsuta 4259, Midori-ku, Yokohama 226-8503, Japan, Department of Electronic Chemistry, Interdisciplinary Graduate School of Science and Engineering, Tokyo Institute of Technology, Nagatsuta 4259, Midori-ku, Yokohama 226-8503, Japan, Department of Chemistry and Bioscience, Kurashiki University of Science and the Arts Nishinoura 2640, Tsurajima, Kurashiki, 712-8505, Japan, Core Research for Evolutional Science and Technology, Japan Science and Technology Corp. (CREST, JST), 2-1-13 Higashiueno, Taito-ku, Tokyo 110-0015

Received: September 28, 2003; In Final Form: November 28, 2003

The series $\text{Ln}_2\text{Ti}_2\text{S}_2\text{O}_5$ ($\text{Ln} = \text{Pr, Nd, Sm, Gd, Tb, Dy, Ho}$ and Er) is demonstrated to evolve H_2 or O_2 from aqueous solutions under visible-light ($440 \text{ nm} \leq \lambda \leq 650 \text{ nm}$) irradiation in the presence of a sacrificial electron donor ($\text{Na}_2\text{S}-\text{Na}_2\text{SO}_3$) or acceptor (Ag^+) without noticeable degradation. $\text{Ln}_2\text{Ti}_2\text{S}_2\text{O}_5$ is synthesized by sulfurization under H_2S flow, and the $\text{Sm}_2\text{Ti}_2\text{S}_2\text{O}_5$ form is found to have the highest activity for O_2 evolution. X-ray Rietveld refinements reveal that the $\text{Ln}_2\text{Ti}_2\text{S}_2\text{O}_5$ framework of the Pr , Nd , and Er forms is distorted from the ideal perovskite structure. The calculations of the electronic band structures of $\text{Ln}_2\text{Ti}_2\text{S}_2\text{O}_5$ based on plane-wave based density functional theory indicated that the top of the valence band of $[\text{Gd}-\text{Er}]_2\text{Ti}_2\text{S}_2\text{O}_5$ is made up of hybridized $\text{O}2\text{p}$, $\text{S}3\text{p}$, and $\text{Ln}4\text{f}$ orbitals, whereas $\text{Ln}4\text{f}$ orbitals are localized in other $[\text{Pr}-\text{Sm}]_2\text{Ti}_2\text{S}_2\text{O}_5$. In addition, the conduction band of $[\text{Gd}-\text{Er}]_2\text{Ti}_2\text{S}_2\text{O}_5$ consists of $\text{S}3\text{p}+\text{Ln}4\text{f}$ and $\text{Ti}3\text{d}$ orbitals. The photocatalytic activity is discussed on the basis of the electronic band structure and bulk material structure.

Introduction

Photocatalysts for overall water splitting have great potential for solar energy applications. A range of oxide semiconductors with ultraviolet-light response function as stable photocatalysts for overall water splitting to generate stoichiometric H_2 and O_2 .^{1–3} These materials are, however, not active under visible light. The development of photocatalysts with visible-light response would therefore be valuable for application to H_2 production using solar energy. The present authors have already reported that the oxysulfide $\text{Sm}_2\text{Ti}_2\text{S}_2\text{O}_5$ functions as a stable photocatalyst for the reduction of H^+ to H_2 and oxidation of H_2O to O_2 in the presence of a sacrificial electron donor and acceptor under visible-light irradiation.⁴ A new synthetic route to $\text{Sm}_2\text{Ti}_2\text{S}_2\text{O}_5$ using H_2S has also been reported.⁵ Recently, the series $\text{Ln}_2\text{Ti}_2\text{S}_2\text{O}_5$ ($\text{Ln} = \text{Pr, Nd, Sm, Gd, Tb, Dy, Ho}$, and Er) has been synthesized by Boyer-Candalen et al.,⁶ and it is expected that the members of this $\text{Ln}_2\text{Ti}_2\text{S}_2\text{O}_5$ series will also function as visible light-responsive photocatalysts. This paper reports a new synthetic route to $\text{Ln}_2\text{Ti}_2\text{S}_2\text{O}_5$ using H_2S and discusses the photocatalytic activities of $\text{Ln}_2\text{Ti}_2\text{S}_2\text{O}_5$ on the basis of band-structure calculations and crystal structures determined by X-ray diffraction (XRD) analysis.

Experimental Section

Synthesis of $\text{Ln}_2\text{Ti}_2\text{S}_2\text{O}_5$. $\text{Ln}_2\text{Ti}_2\text{S}_2\text{O}_5$ was synthesized by two methods. The first method involved a solid-state reaction, as can be found in the literature.^{6,7} By this method, $\text{Ln}_2\text{Ti}_2\text{S}_2\text{O}_5$ samples were obtained by heating a mixture of Ln_2S_3 (99.999%, Soekawa Chemical Co., Ltd.), Ln_2O_3 , and TiO_2 (99.95%, 98.5%, Kanto Chemical Co., Inc.) at a molar ratio of 2:1:6 (Ln_2S_3 : Ln_2O_3 : TiO_2) in a sealed quartz tube under vacuum at 1273 K. After 1 week, the sintered samples were ground and heated in the vacuum-sealed tube for an additional week. The obtained samples were finally ground into powders. This synthesis method is abbreviated as the solid-state reaction (“SSR”) method. The obtained samples were used for structure refinement. The other method involved the sulfurization reaction of lanthanoid titanate under H_2S flow. Precursors, that is, the lanthanoid titanates, to be sulfurized under flowing H_2S were prepared by the polymerized complex method⁸ using $\text{Ti}(\text{OiPr})_4$ and $\text{Ln}(\text{NO}_3)_3 \cdot 6\text{H}_2\text{O}$ as starting materials. Ethylene glycol and methanol were used as solvents, and anhydrous citric acid was employed as a complexing agent to stabilize Ti and Ln ions. After polymerization of the mixture containing Ti and Ln ions according to the method in the literature,⁷ lanthanoid titanates were obtained by calcination at 773 K in air. The obtained samples are labeled as “oxide precursor” samples. $\text{Ln}_2\text{Ti}_2\text{S}_2\text{O}_5$ was prepared from the oxide precursor (0.5 g) by calcination under flowing H_2S (flow rate: 10 mL/min) at various temperatures and for sulfurization times. This synthesis method is abbreviated as the H_2S -gas sulfurization (“HGS”) method. The obtained samples were used for photocatalytic reactions because

* To whom correspondence should be addressed. E-mail: kdomen@res.titech.ac.jp.

[†] Chemical Resources Laboratory, Tokyo Institute of Technology.

[‡] Department of Electronic Chemistry, Interdisciplinary Graduate School of Science and Engineering, Tokyo Institute of Technology.

[§] Department of Chemistry and Bioscience, Kurashiki University of Science and the Arts.

^{||} CREST, JST.

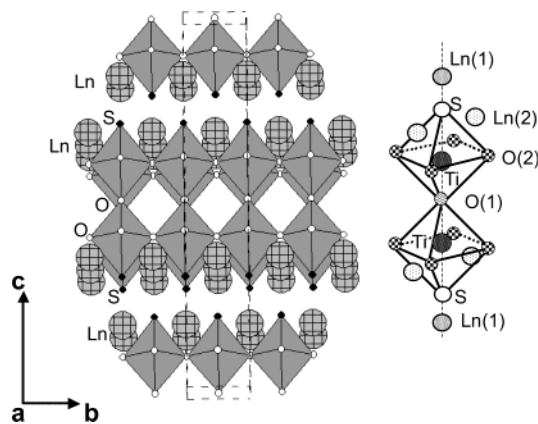


Figure 1. Schematic structure of the $\text{Ln}_2\text{Ti}_2\text{S}_2\text{O}_5$ structure.

the HGS method could produce $\text{Ln}_2\text{Ti}_2\text{S}_2\text{O}_5$ with superior photocatalytic activity compared to the solid-state method.

Characterization of Catalysts. The obtained samples were characterized by X-ray powder diffraction Geigerflex RAD-B, Rigaku; Cu $K\alpha$), field-emission scanning electron microscopy (FE-SEM; S-4700, Hitachi), energy-dispersive X-ray spectroscopy (EDX; Emax-7000, Horiba), and ultraviolet–visible diffuse reflectance spectroscopy (UV–vis DRS; V-560, JASCO).

Photocatalytic Reactions. The reactions were carried out in a Pyrex reaction vessel connected to a closed gas circulation and evacuation system. Photoreduction of H^+ to H_2 and photooxidation of H_2O to O_2 in the presence of a sacrificial electron donor and acceptor were examined as test photoreactions. The photooxidation of water to O_2 was performed in 200 mL of 0.01 M AgNO_3 solution (Ag^+ as the sacrificial electron acceptor) containing 0.20 g of $\text{Ln}_2\text{Ti}_2\text{S}_2\text{O}_5$ and 0.20 g of La_2O_3 powder. Photooxidation of water lowers the pH of the solution because H^+ is produced during O_2 evolution. In the presence of La_2O_3 , the pH of the solution during the photoreactions was buffered at pH = 8–9 by dissolution of La_2O_3 or $\text{La}(\text{OH})_3$, a basic metal oxide. For H_2 evolution, Pt was loaded by the impregnation method from H_2PtCl_6 , followed by reduction in H_2 at 473 K. H_2 evolution was typically examined in a 200 mL aqueous solution containing 0.20 g of $\text{Ln}_2\text{Ti}_2\text{S}_2\text{O}_5$ loaded with 1.0 wt % Pt and sacrificial electron donors (0.01 M Na_2S –0.01 M Na_2SO_3). To remove air from the reactor, the solution was evacuated several times and then irradiated with a 300 W Xe lamp equipped with cutoff filters. The number of photons reaching the solution was measured using an Si photodiode: the rate of total incident photons at $440 \text{ nm} \leq \lambda \leq 650 \text{ nm}$ was typically $8.6 \times 10^{21} \text{ photons h}^{-1}$. Quantum efficiencies (Φ) were calculated using the following equation.

$$\Phi (\%) = (AR/I) \times 100$$

where A , R , and I are coefficients dependent on the reaction (H_2 evolution, 2; O_2 evolution, 4), the H_2 or O_2 evolution rate (molecules h^{-1}), and the rate of absorption of incident photons, respectively. Here, Φ is the apparent quantum efficiency, where it is assumed that all incident photons are absorbed by the suspension.

Results and Discussion

Structure Refinement. Figure 1 shows the schematic structures of $\text{Ln}_2\text{Ti}_2\text{S}_2\text{O}_5$. The crystal system of $\text{Ln}_2\text{Ti}_2\text{S}_2\text{O}_5$ is tetragonal with space group $I4/mmm$. The atomic coordinates of $\text{Ln}_2\text{Ti}_2\text{S}_2\text{O}_5$ were refined by Rietveld analysis using the computer program RIETAN-2000.⁹ The diffraction data were

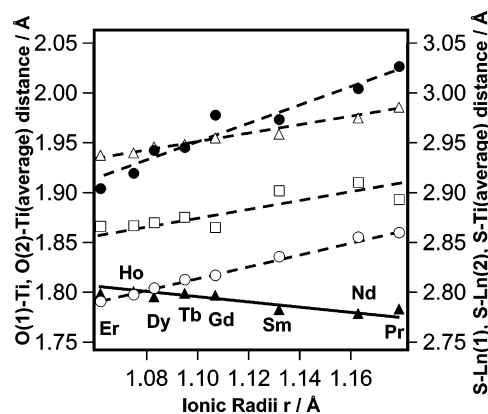


Figure 2. Relationships between ionic radii and O–Ti, S–Ln, and S–Ti bond distances: O(1)–Ti, closed triangles; O(2)–Ti, opened triangles; S–Ln(1), closed circles; S–Ln(2), opened circles; S–Ti, opened squares.

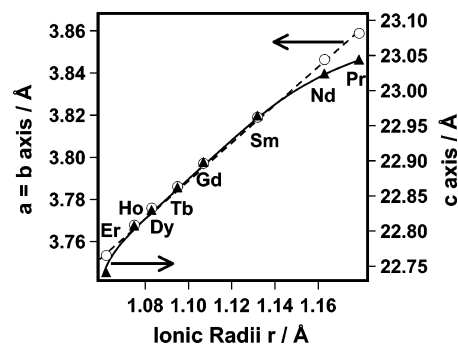


Figure 3. Relationships between ionic radii and lattice parameters of $\text{Ln}_2\text{Ti}_2\text{S}_2\text{O}_5$: $a = b$ axis, closed triangles; c axis, opened circles.

collected for 3 s at each 0.03° step over a 2θ range of 10 – 120° . These refinements gave agreement factors of $R_p = 6.67$ – 9.70% , $R_{wp} = 9.65$ – 15.8% , and $S = R_{wp}/R_e = 1.3$ – 1.9 . The estimated atomic coordinates of $\text{Ln}_2\text{Ti}_2\text{S}_2\text{O}_5$ were in good agreement with those in the literature.^{6,10}

Figure 2 shows the relationship between the ionic radii of 9-coordinated Ln^{3+} ions¹¹ and O(1)–Ti, O(2)–Ti, Ln(1)–S, Ln(2)–S, and Ti–S distances taken from the X-ray Rietveld refinement results for $\text{Ln}_2\text{Ti}_2\text{S}_2\text{O}_5$. All binding distances except for O(1)–Ti increased with increasing ionic radii of the Ln^{3+} ions, indicating that a change in the O(1)–Ti distance gives rise to distortion of the TiSO_5 octahedra. The rate of Ln(1)–S lengthening also differed from that for Ln(1)–S, Ti–S, or O(2)–Ti. The change in the Ln(1)–S distance appears to be related to the change in O(1)–Ti.

Figure 3 shows the relationship between the lattice constants of $\text{Ln}_2\text{Ti}_2\text{S}_2\text{O}_5$ and the ionic radii of Ln^{3+} ions. In $\text{Ln}_2\text{Ti}_2\text{S}_2\text{O}_5$ (Ln = Er, Ho, Dy, Tb, Gd, Sm, Nd, and Pr), the a and b axis distances of the lattice constants increased linearly with increasing ionic radii of the lanthanoid ions, from Er to Pr. Although the c -axis distance increased with the ionic radius, the increase was not linear. It is considered that this change in the c axis distance is caused by an increase or decrease in the O(1)–Ti and Ln(1)–S distances. The X-ray Rietveld refinement results therefore imply that the structure of $[\text{Pr}, \text{Nd}, \text{Er}]_2\text{Ti}_2\text{S}_2\text{O}_5$ is distorted from the ideal perovskite structure.

Electronic Structure Calculations. The series $\text{Ln}_2\text{Ti}_2\text{S}_2\text{O}_5$ was further investigated by calculating the band structure on the basis of plane-wave density functional theory (DFT) using CASTEP.¹² The atomic coordinates of $\text{Ln}_2\text{Ti}_2\text{S}_2\text{O}_5$ refined by the Rietveld analysis were used in the DFT calculations. The core orbitals were replaced by the ultrasoft core potentials,¹³

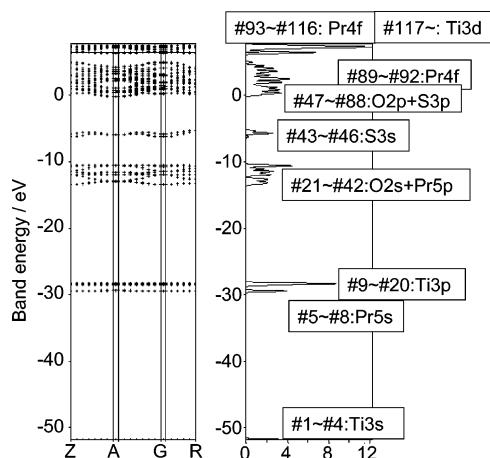


Figure 4. Band dispersion and density of states for $\text{Pr}_2\text{Ti}_2\text{S}_2\text{O}_5$.

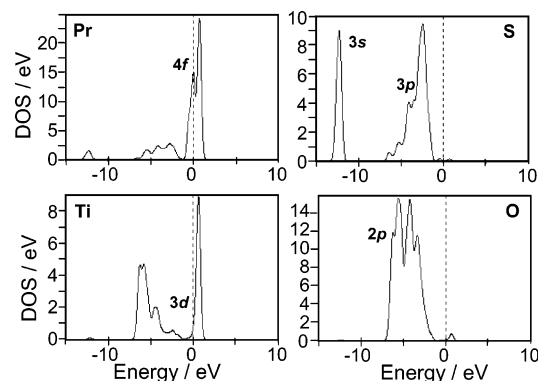


Figure 5. Partial DOS for $\text{Pr}_2\text{Ti}_2\text{S}_2\text{O}_5$.

and the $\text{O}2s^22p^4$, $\text{S}3s^23p^4$, $\text{Ti}3s^23p^63d^24s^2$, and $\text{Ln}(\text{Pr}5s^25p^64f^36s^2, \text{Nd}5s^25p^64f^46s^2, \text{Sm}5s^25p^64f^66s^2, \text{Gd}4f^75d^16s^2, \text{Tb}4f^96s^2, \text{Dy}4f^{10}6s^2, \text{Ho}4f^{11}6s^2, \text{Er}4f^{12}6s^2)$ electrons were treated explicitly. The kinetic energy cutoff was set at 280 eV. As the $\text{Ln}4f$ orbitals ($\text{Ln} = \text{Pr} - \text{Er}$) have smaller overlap and lower ionization potential, the self-consistent field (SCF) convergence was not good. Therefore, a fractional occupation technique was employed, which allows for the withdrawal and accumulation of a small amount of electron density in the top of the valence band and bottom of the conduction band. The calculated band dispersions and densities of states for $\text{Pr}_2\text{Ti}_2\text{S}_2\text{O}_5$ are shown in Figure 4. The top of the valence band corresponds to orbital #92, and the bottom of the conduction band corresponds to orbital #93. The contents of each band are shown in Figure 4. For example, orbitals #47 to #88 are composed of $\text{O}2p$ and $\text{S}3p$ orbitals. The band gap, which is apparently very small, lies between orbitals #92 and #93. The partial DOS for $\text{Pr}_2\text{Ti}_2\text{S}_2\text{O}_5$ are also shown in Figure 5 in the energy region from -15 to $+10$ eV, where the Fermi level is set to zero on the abscissa. The valence band is made up of hybridized $\text{O}2p$ and $\text{S}3p$ orbitals and then localized $\text{Pr}4f$ orbitals, whereas the conduction band starts with localized $\text{Pr}4f$ orbitals and then $\text{Ti}3d$ orbitals. The valence band also contains small contributions from $\text{Ti}3d$ orbitals by the overlap with $\text{O}2p$ and $\text{S}3p$ orbitals. Except for just the top of the valence band, the higher energy region is occupied by $\text{S}3p$ orbitals and the lower energy region is occupied by $\text{O}2p$ orbitals. Although the $\text{Pr}4f$ orbitals appear both at the top of the valence band and at the bottom of the conduction band, the $4f$ orbitals are relatively localized and the overlap between $4f$ orbitals is small. In our understanding, even if the $4f$ orbitals accept electrons by visible-light irradiation, it is less effective to transfer those electrons to the catalyst surface

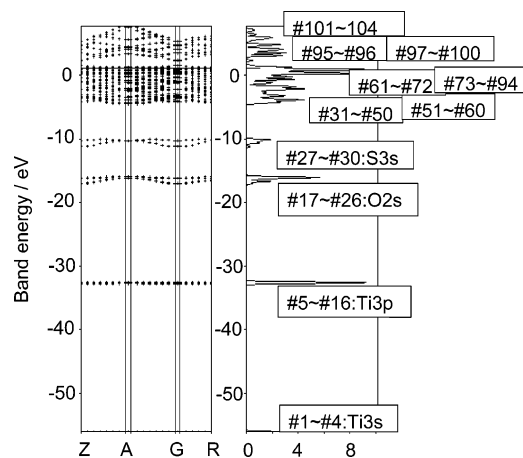


Figure 6. Band dispersion and density of states for $\text{Er}_2\text{Ti}_2\text{S}_2\text{O}_5$: #31–#50, $\text{O}2p$; #51–#60, $\text{O}2p + \text{S}3p$; #61–#72, $\text{O}2p + \text{S}3p + \text{Er}4f$; #73–#94, $\text{Er}4f$; #95–#96, $\text{Er}4f$; #97–#100, $\text{S}3p + \text{Er}4f$; #101–#104, $\text{Ti}3d$.

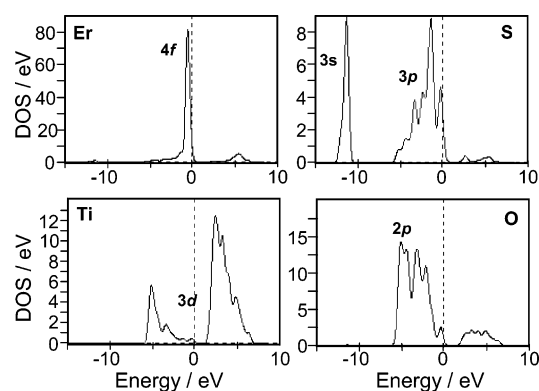


Figure 7. Partial DOS for $\text{Er}_2\text{Ti}_2\text{S}_2\text{O}_5$.

and the materials reduced. The $4f$ orbitals can contribute to the photocatalytic activities by hybridization with the $\text{S}3p$ and $\text{O}2p$ orbitals, that is, rather indirect fashion. Thus, the band gap is reasonably estimated to be 2.46 eV, taken as the energy difference between the top of the $\text{O}2p + \text{S}3p$ band and the bottom of the $\text{Ti}3d$ band.

The calculated band dispersions and densities of states for $\text{Er}_2\text{Ti}_2\text{S}_2\text{O}_5$ are shown in Figure 6. The top of the valence band corresponds to orbital #94, and the bottom of the conduction band corresponds to orbital #95. Figure 7 shows the partial DOS for $\text{Er}_2\text{Ti}_2\text{S}_2\text{O}_5$ for the width of 25 eV in the band gap region. The valence band is made up of $\text{O}2p + \text{S}3p$, $\text{O}2p + \text{S}3p + \text{Er}4f$, and $\text{Er}4f$ (partial), in increasing order of energy. The valence band also contains small contributions from $\text{Ti}3d$ orbitals by the overlap with $\text{O}2p$ and $\text{S}3p$ orbitals. The band structure of $\text{Er}_2\text{Ti}_2\text{S}_2\text{O}_5$ differs on two points from that of $\text{Pr}_2\text{Ti}_2\text{S}_2\text{O}_5$; hybridization of the $\text{O}2p$, $\text{S}3p$, and $\text{Er}4f$ orbitals, as shown in Figure 7, and the contents of the conduction band or the relative location of $4f$ orbitals. Although it is difficult to recognize the small fraction of $\text{Er}4f$ in the conduction band in Figure 7 because of the stronger peak of $\text{Er}4f$ in the valence band, the unoccupied bands consist of $\text{Er}4f$ (partial), $\text{S}3p + \text{Er}4f$, and $\text{Ti}3d$, as shown in Figure 6. The band gap is reasonably estimated to be 0.87 eV, taken as the energy difference between the top of the $\text{O}2p + \text{S}3p + \text{Er}4f$ band and the bottom of the $\text{S}3p + \text{Er}4f$ band.

The electronic structure changes gradually over the lanthanoid series. The two largest changes are lowering of the $\text{Ln}4f$ band energy and increasing hybridization along with the increase of $4f$ electron number. In the papers by Machida et al., LnTaO_4 ($\text{Ln} = \text{La}, \text{Ce}, \text{Pr}, \text{Nd}, \text{and Sm}$)¹⁴ and $\text{RbLnTa}_2\text{O}_7$ ($\text{Ln} = \text{La},$

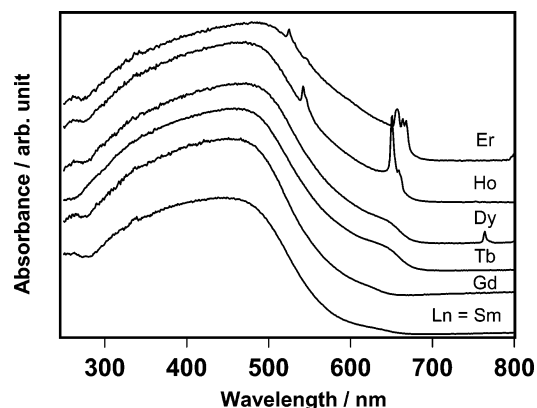


Figure 8. UV-vis diffuse reflectance spectra of $\text{Ln}_2\text{Ti}_2\text{S}_2\text{O}_5$ ($\text{Ln} = \text{Sm}, \text{Gd}, \text{Tb}, \text{Dy}, \text{Ho}$ and Er).

TABLE 1: Optical Bandgap of $\text{Ln}_2\text{Ti}_2\text{S}_2\text{O}_5$

compound	band gap (eV)
$\text{Sm}_2\text{Ti}_2\text{S}_2\text{O}_5$	2.13
$\text{Gd}_2\text{Ti}_2\text{S}_2\text{O}_5$	2.09
$\text{Tb}_2\text{Ti}_2\text{S}_2\text{O}_5$	2.04
$\text{Dy}_2\text{Ti}_2\text{S}_2\text{O}_5$	2.00
$\text{Ho}_2\text{Ti}_2\text{S}_2\text{O}_5$	1.98
$\text{Er}_2\text{Ti}_2\text{S}_2\text{O}_5$	1.94

Pr , Nd , and Sm)¹⁵ are treated. The lowering of the $\text{Ln}4f$ band energy over the lanthanoid series was also reported. In this point, our result is consistent with them. Just the top of the valence band and just the bottom of the conduction band consist of solely $4f$ orbitals for all the $\text{Ln}_2\text{Ti}_2\text{S}_2\text{O}_5$ compounds. However, for the earlier lanthanoid elements such as Pr , $\text{Pr}4f$ orbitals do not mix with $\text{O}2p$ and $\text{S}3p$ orbitals in the valence band and conduction band. For the late lanthanoid elements such as Er , $\text{Er}4f$ orbitals mix with $\text{O}2p$ and $\text{S}3p$ orbitals in the valence band and mix with $\text{S}3p$ orbitals in the conduction band. The latter is caused by a lowering of $4f$ orbital energy.

The DFT calculations revealed that the series $\text{Ln}_2\text{Ti}_2\text{S}_2\text{O}_5$ can be separated into two groups according to the electronic band structure. $\text{Nd}_2\text{Ti}_2\text{S}_2\text{O}_5$ and $\text{Sm}_2\text{Ti}_2\text{S}_2\text{O}_5$ have the same electronic band structures as $\text{Pr}_2\text{Ti}_2\text{S}_2\text{O}_5$, whereas the Gd , Tb , Dy , Ho , and Er forms represent a different structurally similar group. In the case of the Pr , Nd , and Sm forms, the valence band is made up of hybridized $\text{O}2p$ and $\text{S}3p$ orbitals and separated $\text{Ln}4f$ orbitals to the higher energy region, and the conduction band consists of separated $\text{Ln}4f$ orbitals to lower energy region and $\text{Ti}3d$ orbitals. On the other hand, the top of the valence band for the Gd – Er group is made up of hybridized $\text{O}2p$, $\text{S}3p$ and $\text{Ln}4f$ orbitals and the conduction band consists of $\text{S}3p$ + $\text{Ln}4f$ and $\text{Ti}3d$ orbitals.

The diffuse reflectance spectra of $[\text{Sm}, \text{Gd}, \text{Tb}, \text{Dy}, \text{Ho}, \text{Er}]_2\text{Ti}_2\text{S}_2\text{O}_5$ are shown in Figure 8. The Tb , Dy , Ho , and Er forms exhibit a weak absorption band at 600–700 nm due to an f – f transition. The band gap energies calculated from the absorption band-edge positions, excepting the f – f transition, are summarized in Table 1. The band gap energies of $\text{Ln}_2\text{Ti}_2\text{S}_2\text{O}_5$ decrease with increasing atomic number of the lanthanoid ions from Sm^{3+} to Er^{3+} . It is considered that the $\text{O}2p$ + $\text{S}3p$ + $\text{Ln}4f$ and $\text{S}3p$ + $\text{Ln}4f$ hybridized orbitals in the valence and conduction bands for the Gd , Tb , Dy , Ho , and Er forms gives rise to this decrease in band gap energy.

Crystal Forms of $\text{Ln}_2\text{Ti}_2\text{S}_2\text{O}_5$ Prepared by H_2S -Gas Sulfurization. The authors have previously reported the advantages of the new synthetic route to $\text{Sm}_2\text{Ti}_2\text{S}_2\text{O}_5$ using H_2S with respect to preparation of active photocatalysts.⁵ For the

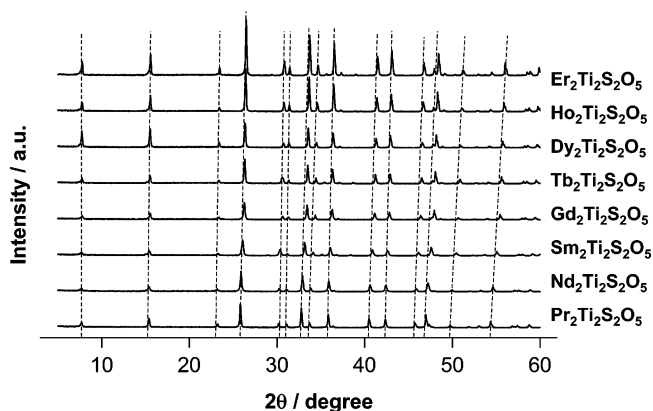


Figure 9. XRD patterns for $\text{Ln}_2\text{Ti}_2\text{S}_2\text{O}_5$ (HGS).

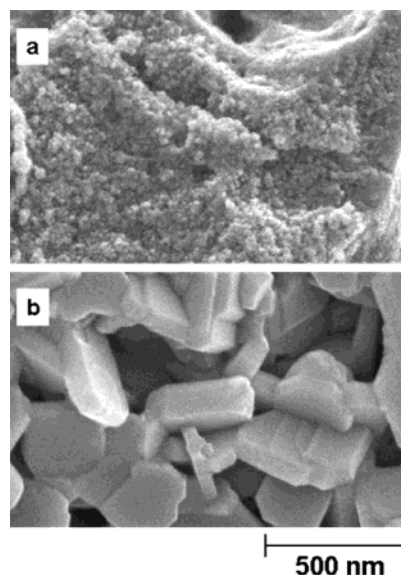


Figure 10. SEM images of (a) amorphous $\text{Gd}_2\text{Ti}_2\text{O}_7$ and (b) $\text{Gd}_2\text{Ti}_2\text{S}_2\text{O}_5$ (HGS).

HGS synthesis reported here, the optimal conditions for sulfurization of $\text{Ln}_2\text{Ti}_2\text{O}_7$ are determined on the basis of the photocatalytic activity for O_2 evolution. Figure 9 shows the XRD patterns of $\text{Ln}_2\text{Ti}_2\text{S}_2\text{O}_5$ obtained by sulfurization of the various amorphous oxide precursors at 1173–1273 K for 1–4 h. The products obtained consisted of a single $\text{Ln}_2\text{Ti}_2\text{S}_2\text{O}_5$ phase. The sulfur content in the Er , Nd , and Pr forms of $\text{Ln}_2\text{Ti}_2\text{S}_2\text{O}_5$ were, however, slightly lower than in the other $\text{Ln}_2\text{Ti}_2\text{S}_2\text{O}_5$ forms, as determined by EDX analysis.

Figure 10 shows SEM images of amorphous $\text{Gd}_2\text{Ti}_2\text{O}_7$ and $\text{Gd}_2\text{Ti}_2\text{S}_2\text{O}_5$ (HGS). $\text{Gd}_2\text{Ti}_2\text{O}_7$ was granular with an uneven surface, and individual particles are clearly distinguishable. The surface area of the amorphous $\text{Gd}_2\text{Ti}_2\text{O}_7$ was $50 \text{ m}^2 \text{ g}^{-1}$. Similar morphologies were observed for the other oxide precursors. $\text{Gd}_2\text{Ti}_2\text{S}_2\text{O}_5$ (HGS) was observed to consist of platelike particles and have a flat surface. This morphology was also common to all other HGS samples. The surface area of the $\text{Gd}_2\text{Ti}_2\text{S}_2\text{O}_5$ (HGS) sample was $6 \text{ m}^2 \text{ g}^{-1}$, and although this surface area is significantly lower than for the precursor, the value is 10 times that of samples prepared by the SSR method ($0.6 \text{ m}^2 \text{ g}^{-1}$).

Photocatalytic Activity of $\text{Ln}_2\text{Ti}_2\text{S}_2\text{O}_5$ under Visible Light Irradiation. Heating $\text{Sm}_2\text{Ti}_2\text{S}_2\text{O}_5$ in air at 473 K for 2 h has been found to enhance the photocatalytic activity of this catalyst for both H_2 and O_2 evolution through the oxidation of surface S^0 species.⁵ In the case of $\text{Ln}_2\text{Ti}_2\text{S}_2\text{O}_5$, heat treatment again enhanced the photocatalytic activities. Table 2 lists the photo-

TABLE 2: Photocatalytic Activity of $\text{Ln}_2\text{Ti}_2\text{S}_2\text{O}_5$

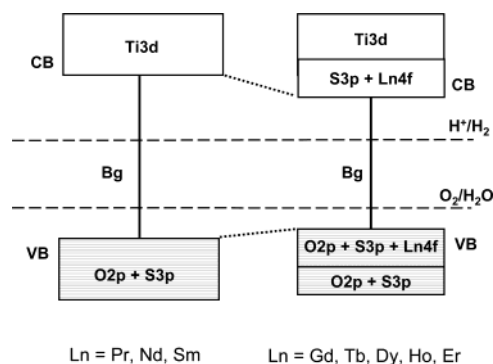
compound	rate of O_2 evol, $\mu\text{mol/h}$	rate of H_2 evol, $\mu\text{mol/h}$
$\text{Pr}_2\text{Ti}_2\text{S}_2\text{O}_5$	0	0
$\text{Nd}_2\text{Ti}_2\text{S}_2\text{O}_5$	3	4
$\text{Sm}_2\text{Ti}_2\text{S}_2\text{O}_5$	22	22
$\text{Gd}_2\text{Ti}_2\text{S}_2\text{O}_5$	21	24
$\text{Tb}_2\text{Ti}_2\text{S}_2\text{O}_5$	20	19
$\text{Dy}_2\text{Ti}_2\text{S}_2\text{O}_5$	9	10
$\text{Ho}_2\text{Ti}_2\text{S}_2\text{O}_5$	5	22
$\text{Er}_2\text{Ti}_2\text{S}_2\text{O}_5$	1	21

catalytic activities of heat-treated $\text{Ln}_2\text{Ti}_2\text{S}_2\text{O}_5$ (HGS) for the reduction of H^+ to H_2 and oxidation of H_2O to O_2 in the presence of a sacrificial electron donor or acceptor. O_2 evolution was examined in a basic solution (ca. pH = 8) buffered with La_2O_3 . In this reaction, the rate of O_2 evolution decreased with reaction time due to deposition of metallic silver on the surface of the catalyst, effectively shielding the catalyst from incident light. Therefore, the initial rate of O_2 evolution was regarded as the activity. The highest activity for O_2 evolution was obtained for $\text{Sm}_2\text{Ti}_2\text{S}_2\text{O}_5$, with an estimated quantum efficiency of 0.7%. The pH of the aqueous Na_2S – Na_2SO_3 solution for H_2 evolution was 13. Platinum as an H_2 evolution promoter was loaded by the impregnation method from H_2PtCl_6 , followed by reduction under H_2 at 473 K. The rate of H_2 evolution was stable, and the steady H_2 evolution rates are shown in Table 2. The highest activity for H_2 evolution was obtained for $\text{Gd}_2\text{Ti}_2\text{S}_2\text{O}_5$, with a steady-state quantum efficiency of 0.1%.

Relationship between Photocatalytic Activity and Band Structure. The optimal conditions for sulfurization of $\text{Ln}_2\text{Ti}_2\text{O}_7$ in the HGS method were determined on the basis of the photocatalytic activity of O_2 evolution and may not be optimal for H_2 evolution. Therefore, the photocatalytic activities of O_2 evolution are discussed here. The photocatalytic activity for the oxidation of water in the presence of a sacrificial acceptor can be summarized by the order $\text{Pr}_2\text{Ti}_2\text{S}_2\text{O}_5 < \text{Nd}_2\text{Ti}_2\text{S}_2\text{O}_5 \ll \text{Sm}_2\text{Ti}_2\text{S}_2\text{O}_5 > \text{Gd}_2\text{Ti}_2\text{S}_2\text{O}_5 > \text{Tb}_2\text{Ti}_2\text{S}_2\text{O}_5 > \text{Dy}_2\text{Ti}_2\text{S}_2\text{O}_5 > \text{Ho}_2\text{Ti}_2\text{S}_2\text{O}_5 \gg \text{Er}_2\text{Ti}_2\text{S}_2\text{O}_5$. The highest activity for O_2 evolution was obtained for $\text{Sm}_2\text{Ti}_2\text{S}_2\text{O}_5$.

The structural refinements implied that the frameworks of $[\text{Pr},\text{Nd},\text{Er}]_2\text{Ti}_2\text{S}_2\text{O}_5$ are distorted from the ideal perovskite structure. The colors of these materials were black, dark brown, and dark brown, respectively, whereas the other $\text{Ln}_2\text{Ti}_2\text{S}_2\text{O}_5$ forms were orange. Furthermore, EDX analysis revealed the S content in the Pr, Nd, and Er forms to be slightly lower than that in the other $\text{Ln}_2\text{Ti}_2\text{S}_2\text{O}_5$ forms. Apparently, $[\text{Pr},\text{Nd},\text{Er}]_2\text{Ti}_2\text{S}_2\text{O}_5$ contains larger amounts of sulfur defects than other oxysulfides, resulting in the distortion. Many sulfur defects in $[\text{Pr},\text{Nd},\text{Er}]_2\text{Ti}_2\text{S}_2\text{O}_5$ probably arise from difference in ionic radius: the ionic radiuses of Pr^{3+} and Nd^{3+} (Pr^{3+} , 1.179 nm; Nd^{3+} , 1.163 nm) are larger than that of Sm^{3+} – Ho^{3+} (1.132–1.072 nm), whereas Er^{3+} (1.062 nm) has a smaller radius than Sm^{3+} . Because distorted structures in metal oxide photocatalyst often stimulate efficient charge separation,^{16–19} the low photocatalytic activities of $[\text{Pr},\text{Nd},\text{Er}]_2\text{Ti}_2\text{S}_2\text{O}_5$ can be attributed to the sulfur defects, rather than distortion.

Figure 11 shows the schematic band structure of $\text{Ln}_2\text{Ti}_2\text{S}_2\text{O}_5$. DFT calculations indicated that the top of the valence band of $[\text{Gd}–\text{Er}]_2\text{Ti}_2\text{S}_2\text{O}_5$ is made up of hybridized $\text{O}2\text{p}$, $\text{S}3\text{p}$, and $\text{Ln}4\text{f}$ orbitals, whereas $\text{Ln}4\text{f}$ orbitals are localized in other $[\text{Pr}–\text{Sm}]_2\text{Ti}_2\text{S}_2\text{O}_5$. In addition, the conduction band of $[\text{Gd}–\text{Er}]_2\text{Ti}_2\text{S}_2\text{O}_5$ consists of $\text{S}3\text{p} + \text{Er}4\text{f}$ and $\text{Ti}3\text{d}$ orbitals. The band gap energies of $\text{Ln}_2\text{Ti}_2\text{S}_2\text{O}_5$ decrease with increasing atomic number of the lanthanoid ions from Sm^{3+} to Er^{3+} due to the occurrence of these hybridized orbitals. The difference between

**Figure 11.** Schematic band structure of $\text{Ln}_2\text{Ti}_2\text{S}_2\text{O}_5$.

the oxidation potential of water and the valence band level of $\text{Sm}_2\text{Ti}_2\text{S}_2\text{O}_5$ is small at pH = 8.⁴ The valence band of $[\text{Gd}–\text{Er}]_2\text{Ti}_2\text{S}_2\text{O}_5$ appears to shift to higher potential energies because of the smaller band gap energy of the Gd–Er forms, and the difference between the oxidation potential of water and the valence band decreases with decreasing band gap energy. It is, therefore, considered that the decrease in photocatalytic activities of $[\text{Gd}–\text{Er}]_2\text{Ti}_2\text{S}_2\text{O}_5$ for the oxidation of H_2O to O_2 is attributed to the thermodynamically less favorable valence band position for water oxidation. On the other hand, the conduction band position seems not to affect the rate of H_2 evolution. According to DFT calculation, the conduction band positions of $\text{Ho}_2\text{Ti}_2\text{S}_2\text{O}_5$ and $\text{Er}_2\text{Ti}_2\text{S}_2\text{O}_5$ are expected to be more positive than that of $\text{Sm}_2\text{Ti}_2\text{S}_2\text{O}_5$, but there is no significant difference in H_2 evolution among these oxysulfides. This means that H_2 evolution cannot be simply attributed to conduction band position in oxysulfides. Such a phenomenon is also observed in oxynitride photocatalysts.^{20–22} TaON has a more positive conduction band potential than Ta_3N_5 , whereas the rate of H_2 evolution is larger than that of Ta_3N_5 .

Conclusion

The results of this study imply that the photocatalytic activity of lanthanoids is governed by electronic band structure. The series of isotopic compounds with the $\text{Ln}_2\text{Ti}_2\text{S}_2\text{O}_5$ composition were confirmed to be stable visible light-driven photocatalysts for the oxidation of water to O_2 or reduction of H^+ to H_2 . The photocatalytic activity of $[\text{Pr},\text{Nd},\text{Er}]_2\text{Ti}_2\text{S}_2\text{O}_5$, containing sulfur defects and Ti as Ti^{3+} , was lower than that of the other $\text{Ln}_2\text{Ti}_2\text{S}_2\text{O}_5$ forms. The band gap energies of $[\text{Gd}–\text{Er}]_2\text{Ti}_2\text{S}_2\text{O}_5$ decreased with increasing atomic number of the lanthanoid ions from Gd^{3+} to Er^{3+} due to the occurrence of the hybridized orbitals. The difference between the oxidation potential of water and the valence band level appears to decrease with decreasing band gap energy. It is considered that the photocatalytic activities of $[\text{Gd}–\text{Er}]_2\text{Ti}_2\text{S}_2\text{O}_5$ for the oxidation of H_2O to O_2 are lower because of thermodynamically less favorable valence band position for water oxidation. The highest activity for O_2 evolution ($\Phi = 0.7\%$) was obtained for $\text{Sm}_2\text{Ti}_2\text{S}_2\text{O}_5$ prepared by the HGS method.

Acknowledgment. This work was supported under the Core Research for Evolutional Science and Technology (CREST) program of the Japan Science and Technology Co. (JST) and The 21st Century COE program of the Ministry of Education, Science, Sports, and Culture of Japan.

References and Notes

- (1) Kudo, A.; Tanaka, K.; Domen, K.; Maruya, K.; Aika, K.; Onishi, T. *J. Catal.* **1988**, *111*, 67.
- (2) Kudo, A.; Kato, H. *Chem. Phys. Lett.* **2000**, *331*, 373.

- (3) Takata, T.; Furumi, Y.; Shinohara, K.; Tanaka, A.; Hara, M.; Kondo, J. N.; Domen, K. *Chem. Mater.* **1997**, *9*, 1063.
- (4) Ishikawa, A.; Takata, T.; Kondo, J. N.; Hara, M.; Kobayashi, H.; Domen, K. *J. Am. Chem. Soc.* **2002**, *124*, 13547.
- (5) Ishikawa, A.; Takata, T.; Kondo, J. N.; Hara, M.; Kobayashi, H.; Domen, K. *Chem. Mater.* **2003**, *15*, 4442.
- (6) Boyer-Candalen, C.; Derouet, J.; Porcher, P.; Moelo, Y.; Meerschaut, A. *J. Solid State Chem.* **2002**, *165*, 228.
- (7) Lafond, A.; Leynaud, O.; Andre, G.; Bouree, F.; Meerschaut, A. *J. Alloys Compds.* **2002**, *338*, 185.
- (8) Kakihana, M. *J. Sol-Gel Sci.* **1996**, *5*, 7.
- (9) Izumi, F.; Ikeda, T. *Mater. Sci. Forum* **2000**, *321–324*, 198.
- (10) Chen, B.-H.; Eichhorn, B.; Wong-Ng, W. *Acta Crystallogr.* **1994**, *C50*, 161.
- (11) Shannon, R. D. *Acta Crystallogr. Sec. A* **1976**, *32*, 751.
- (12) Payne, M. C.; Teter, M. P.; Allan, D. C.; Arias, T. A. *Rev. Mod. Phys.* **1992**, *64*, 1045.
- (13) Vanderbilt, D. *Phys. Rev. B* **1990**, *41*, 7892.
- (14) Machida, M.; Murakami, S.; Kijima, T.; Matsushima, S.; Arai, M. *J. Phys. Chem. B* **2001**, *105*, 3289.
- (15) Machida, M.; Yabunaka, J.; Kijima, T.; Matsushima, S.; Arai, M. *Int. J. Inorg. Mater.* **2001**, *3*, 545.
- (16) Kudo, A.; Okutomi, H.; Kato, H. *Chem. Lett.* **2000**, 1212.
- (17) Kato, H.; Kudo, A. *Catal. Today* **2003**, *78*, 561.
- (18) Ogura, S.; Kohno, M.; Sato, K.; Inoue, Y. *Phys. Chem. Chem. Phys.* **1999**, *1*, 179.
- (19) Sato, J.; Kobayashi, H.; Inoue, Y. *J. Phys. Chem. B* **2003**, *107*, 7970.
- (20) Chun, W. J.; Ishikawa, A.; Fujisawa, H.; Takata, T.; Hara, M.; Kawai, M.; Matsumoto, Y.; Domen, K. *J. Phys. Chem. B* **2003**, *107*, 1798.
- (21) Hitoki, G.; Ishikawa, A.; Takata, T.; Kondo, J. N.; Hara, M.; Domen, K. *Chemistry Lett.* **2002**, 736.
- (22) Hitoki, G.; Takata, T.; Kondo, J. N.; Hara, M.; Kobayashi, H.; Domen, K. *Chem. Commun.* **2002**, 1698.